Check for updates

ADVANCED MATERIALS
www.advmat.de

Scalable Manufacturing of Free-Standing, Strong $Ti_3C_2T_x$ MXene Films with Outstanding Conductivity

*Jizhen Zhang, Na Kong, Simge Uzun, Ariana Levitt, Shayan Seyedin, Peter A. Lynch, Si Qin, Meikang Han, Wenrong Yang, Jingquan Liu, Xungai Wang, Yury Gogotsi, and Joselito M. Razal**

Free-standing films that display high strength and high electrical conductivity are critical for flexible electronics, such as electromagnetic interference (EMI) shielding coatings and current collectors for batteries and supercapacitors. 2D $Ti_3C_2T_x$ flakes are ideal candidates for making conductive films due to their high strength and metallic conductivity. It is, however, challenging to transfer those outstanding properties of single MXene flakes to macroscale films as a result of the small flake size and relatively poor flake alignment that occurs during solution-based processing. Here, a scalable method is shown for the fabrication of strong and highly conducting pure MXene films containing highly aligned large MXene flakes. These films demonstrate record tensile strength up to ≈570 MPa for a 940 nm thick film and electrical conductivity of ≈15 100 S cm^{-1} for a 214 nm thick film, which are both the highest values compared to previously reported pure $Ti_3C_2T_x$ films. These films also exhibit outstanding EMI shielding performance (≈50 dB for a 940 nm thick film) that exceeds other synthetic materials with comparable thickness. MXene films with aligned flakes provide an effective route for producing large-area, high-strength, and high-electrical-conductivity MXene-based films for future electronic applications.

The scalable processing of nanomaterials into free-standing films that possess high electrical conductivity and high mechanical properties is critical for enabling diverse applications including those in the area of flexible electronics, such as supercapacitors,[1,2] electromagnetic interference (EMI) shielding,[3] sensors,[4] and actuators.[5] To produce highly conducting and mechanically strong films from functional nanomaterials, one of the key challenges is to find nanomaterials with inherently high strength and electrical conductivity.[6,7] MXenes, a growing family of 2D nanomaterials that have a general formula of $M_{n+1}X_nT_x$ (n = 1–4), are promising materials for making strong and conductive films.[8,9] Here, M is a transition metal, X is carbon and/or nitrogen, and T_x denotes terminal groups (−OH, −O, and −F). $Ti_3C_2T_x$ MXene in particular is the most studied MXene and has received significant attention especially in energy storage and EMI shielding applications due to its high volumetric capacitance (≈1500 F cm^{-3})[10] and excellent electrical conductivity (up to 14 000 S cm^{-1} reported for ≈1 µm thin films).[11] Due to the presence of terminal groups, MXene flakes readily disperse in aqueous and organic media[12] and thus can be processed into pure MXene films by vacuum-assisted filtration,[10] spray coating,[13] and spin coating.[14]

Single $Ti_3C_2T_x$ flake has been demonstrated to have outstanding Young's modulus (≈330 GPa) and tensile strength (≈17.3 GPa),[15] which suggests that $Ti_3C_2T_x$ is an excellent building block for fabricating strong films. However, tensile strength values above 120 MPa[16] and Young's moduli above 10 GPa[17] have yet to be demonstrated for assembled pure MXene films (Table S1, Supporting Information). To improve the tensile strength of pure MXene films, a wide range of materials, including poly(vinyl alcohol),[11,18,19] rubber,[20] cellulose nanofibers,[17,21,22] bacterial cellulose,[23] aramid nanofibers,[24,25] and graphene oxide[26] have been used in manufacturing of MXene-based composite films (Table S2, Supporting Information). As expected, those additives significantly improved the connection between MXene flakes, resulting in improved mechanical properties relative to pure MXene films. For instance, the tensile strength and Young's modulus of a MXene/cellulose nanofibrils composite film reached 341 MPa

J. Zhang, Dr. S. Seyedin,[+] Dr. P. A. Lynch, Dr. S. Qin, Prof. X. Wang, Prof. J. M. Razal
Institute for Frontier Materials
Deakin University
Geelong, Victoria 3216, Australia
E-mail: joselito.razal@deakin.edu.au
Dr. N. Kong, Dr. W. Yang
School of Life and Environmental Sciences
Deakin University
Geelong, Victoria 3216, Australia
S. Uzun, A. Levitt, Dr. M. Han, Prof. Y. Gogotsi
A.J. Drexel Nanomaterials Institute and Department of Materials Science and Engineering
Drexel University
Philadelphia, PA 19104, USA
Prof. J. Liu
College of Materials Science and Engineering
Institute for Graphene Applied Technology Innovation
Qingdao University
Qingdao 266071, China
The ORCID identification number(s) for the author(s) of this article can be found under https://doi.org/10.1002/adma.202001093.
[+]Present address: Molecular Sciences Research Hub, Imperial College London, London W12 0BZ, UK

DOI: 10.1002/adma.202001093

 © 2020 WILEY-VCH Verlag GmbH & Co. KGaA, Weinheim

and 41.9 GPa,[22] respectively, which are the highest values for MXene-based composite films to date. However, since those binders often intercalate between MXene flakes, the electrical conductivities of the composites films are over two-order of magnitude lower compared to that of pure MXene films.[11] These prior works clearly illustrate the challenge in maintaining high electrical conductivity while improving the strength of MXene films.

Recently, Chen et al.[16] found that processing of $Ti_3C_2T_x$ dispersions with ≈0.1 M hydrochloric acid (HCl) solution triggers the self-assembly of MXene flakes. As a result, $Ti_3C_2T_x$ films displayed high electrical conductivity (up to 10 400 S cm^{-1}) and improved tensile strength from ≈20 to 112 MPa after the HCl treatment.[16] This approach demonstrated the potential to produce pure MXene films with high strength. The lower electrical conductivity and tensile strength values in the case of pure MXene films are partly due to a combination of factors, including small MXene flake size (lateral size of couple of hundred nanometers), defects on MXene flakes due to sonication, voids formed in film due to the imperfect and irregular staking of flakes. Controlling the size, orientation, and packing density of MXene flakes during solution processing is crucial to improve the overall properties of pure MXene films. However, no study has investigated the effect of flake size and orientation of MXene flakes on the properties of their macrostructures.

To address these challenges, we demonstrate high performance free-standing MXene film with both improved strength and electrical conductivity using a blade-coating method without the use of any binders or additives. First, MXene flakes that have average lateral size of 10 ± 2.1 µm are synthesized using large Ti_3AlC_2 MAX phase particles (>10 µm). These large $Ti_3C_2T_x$ flakes in aqueous dispersion formed lyotropic liquid crystals and showed high viscosity and good flowability with increasing shear rate, which enabled the alignment of flakes under shear force during blade coating. As an example, we produced several meters of a continuous, 940 nm thick MXene film that exhibited the highest tensile strength (568 ± 24 MPa) and Young's modulus (20.6 ± 3.1 GPa). Notably, this tensile strength is about 30 times higher than that of pure MXene film (10–20 MPa) produced by vacuum-assisted filtration without any treatment,[18] five times higher than that of HCl treated MXene film[16] and approximately two times higher than those of the best MXene composite films.[27] After vacuum drying at 200 °C for 6 h, the films produced using blade-coating method reached an electrical conductivity value of ≈15 100 S cm^{-1} that is the highest published value to date for MXene films. As a practical application, the high electrical conductivity offers an excellent EMI shielding performance of 47.9 dB for a 940 nm thick film in the X-band (8.2–12.4 GHz).

$Ti_3C_2T_x$ flakes are synthesized by selectively etching aluminum layers from Ti_3AlC_2 MAX phase (Carbon-Ukraine) and subsequently delaminated into monolayer flakes with the assistance of intercalation agents, such as metal ions and organic molecules.[28] Although sonication and sucrose density gradient centrifugation allow size selection of $Ti_3C_2T_x$ flakes,[29] little effort has been made to increase the flake size of as-synthesized $Ti_3C_2T_x$. The size of the $Ti_3C_2T_x$ flakes depends on three main factors: i) the initial size of MAX phase crystals, which directly limits the maximum size of etched $Ti_3C_2T_x$ flakes, ii) the complete etching of aluminum layers inside the large MAX phase,[28] and iii) the effective exfoliation of monolayer $Ti_3C_2T_x$ flakes to avoid vigorous sonication and thus ensuring minimum breakage of $Ti_3C_2T_x$ flakes during delamination.[30] In the present work, we synthesized single-layer $Ti_3C_2T_x$ flakes with average lateral size of 10 ± 2.1 µm using a modified minimally intensive layer delamination (MILD) method[28,30] by preselecting large Ti_3AlC_2 MAX phase particles (those greater than 10 µm) from the as-received MAX phase prior to the selective etching step, as illustrated in **Figure 1**a. The details of the size selection procedure are presented in Figure S1 in the Supporting Information. The predominantly large MAX phase particles required the etching conditions to be slightly modified from the MILD method to improve the etching efficiency and yield. Here, we used a 12 to 1 molar ratio of LiF to Ti_3AlC_2 in 9 M HCl solution and the etching was carried out at 50 °C with constant stirring for 30 h. This modified method led to the spontaneous exfoliation and delamination of multilayer $Ti_3C_2T_x$ flakes when the supernatant pH reached ≈6 after repeated washing (Table S3, Supporting Information). Traces of unreacted MAX phase and multilayer $Ti_3C_2T_x$ were removed by differential centrifugation method.

We confirmed the purity of our sample by the absence of the 2θ peak of MAX phase at ≈39° in the X-ray powder diffraction (XRD) pattern (Figure 1b). The obtained large $Ti_3C_2T_x$ flakes showed the (*002*) peak at $2\theta \approx 6.5°$, which corresponds to a *c* lattice parameter of 27.1 Å, which is in agreement with literature.[30] For comparison, the small size $Ti_3C_2T_x$ samples were produced by probe-sonicating the as-synthesized MXene dispersion for 20 min (refer to details in the experimental section in the Supporting Information). Compared to dispersions consisting of predominantly large MXene flakes, which had a mean lateral size ($\langle l \rangle$) of ≈10 µm (Figure 1c), dispersions consisting of predominantly small flakes had a $\langle l \rangle$ of ≈200 nm (Figure S2b, Supporting Information). Atomic force microscopy (AFM) analysis of a representative large $Ti_3C_2T_x$ flake (l > 12 µm) revealed an average flake thickness ($\langle t \rangle$) of ≈1.7 nm (Figure 1d), indicating successful delamination into single large $Ti_3C_2T_x$ flakes.[15] We note that the thickness of an individual $Ti_3C_2T_x$ flake is reported to be ≈1 nm based on transmission electron microscopy (TEM) studies and density functional theory (DFT) calculations.[31,32] It is known that factors such as AFM imaging mode (e.g., tapping and contact), tip-surface interactions, presence of various surface adsorbents, and trapped interfacial molecules affect the flake thickness measurement. The higher thickness of MXene flake measured from our AFM image could be due to the high sensitivity of our AFM measurement, which detects the surface functional groups and/or adsorbed molecules on and under the flake.[33]

The chemical composition and structure of large and small $Ti_3C_2T_x$ flakes were investigated by X-ray photoelectron spectroscopy (XPS) and Raman spectroscopy. As seen from the high-resolution XPS spectra (Figure 1e), the peaks at 454.9 eV ($sp_{3/2}$) and 461.2 eV ($sp_{1/2}$) represent a contribution from Ti—C bonds, and the peaks at 456.6 and 462.7 eV correspond to Ti—O bonds.[34,35] The weak intensity of the Ti—O bonds means the prepared large and small $Ti_3C_2T_x$ flakes have no sign of oxidation. The strong intensity of C—Ti bonds at 281.5 eV demonstrates the presence of Ti—C bonds of $Ti_3C_2T_x$ while the intensities of C—O (≈286.8 eV) and C=O (≈289.0 eV) peaks

© 2020 WILEY-VCH Verlag GmbH & Co. KGaA, Weinheim

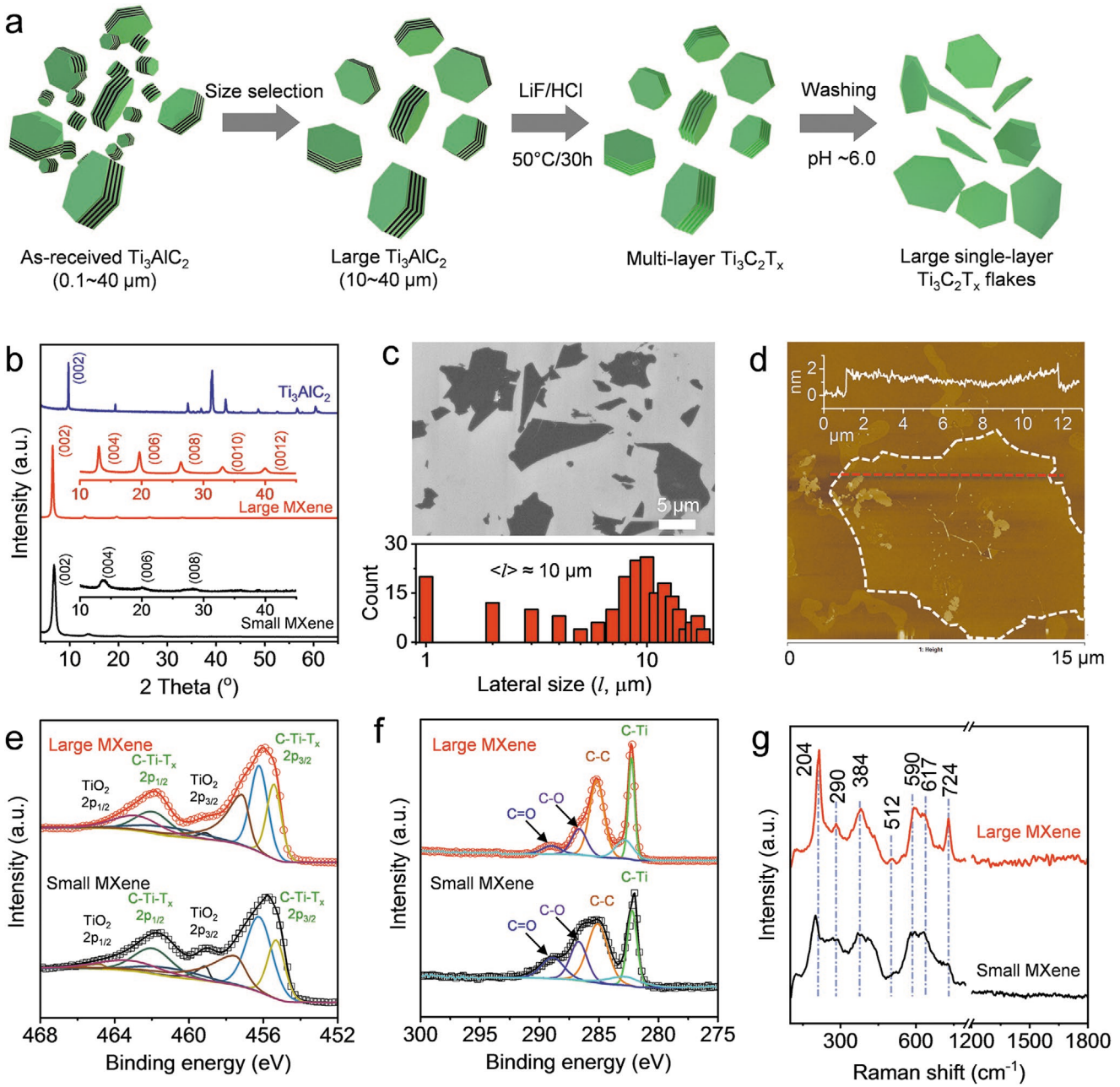


Figure 1. a) The synthesis process of large $Ti_3C_2T_x$ MXene flakes from large Ti_3AlC_2 MAX particles. b) XRD patterns of Ti_3AlC_2 MAX phase powder and drop-cast films made from large and small MXene flakes. c) SEM image of large $Ti_3C_2T_x$ flakes deposited on a silicon wafer. Bottom shows the lateral size distribution of large MXene flakes. d) AFM image of a typical large flake deposited on a silicon substrate. Inset shows the height profile along the dashed red line. e,f) XPS spectra of drop-cast large and small MXene flakes on a silicon wafer showing binding energy values associated with Ti 2p (e) and C 1s (f). g) Raman spectra of large and small MXene flakes drop cast on aluminum foil.

increased slightly for small $Ti_3C_2T_x$ flakes (Figure 1f). The Raman spectra of both large and small flakes are displayed in Figure 1g. Raman fingerprint of $Ti_3C_2T_x$ is located between 100 and 800 cm^{-1} as shown in previous studies.[36,37] Following available Raman vibration predictions,[37] the prominent Raman bands at 204 and 724 cm^{-1} can be assigned to different out-of-plane atom vibration modes (A_{1g}). The stiffer mode is attributed to vibrations of titanium, carbon, and surface groups atoms, whereas the vibration at 724 cm^{-1} is assigned to vibrations of C-atoms. Vibrations between 250 and 500 cm^{-1} are assigned to in-plane vibrations (E_g) of surface group atoms. We also noticed higher intensity of peaks at 204, 384, and 724 cm^{-1} for large $Ti_3C_2T_x$ flakes compared to small flakes, which may be attributed to the increase in flake size and uniform surface functional groups of large MXene flakes, but requires further work to study the effects of flake size and edges on Raman spectra. There are no D and G bands of free carbon observed, which indicates that the samples were not degraded.

© 2020 WILEY-VCH Verlag GmbH & Co. KGaA, Weinheim

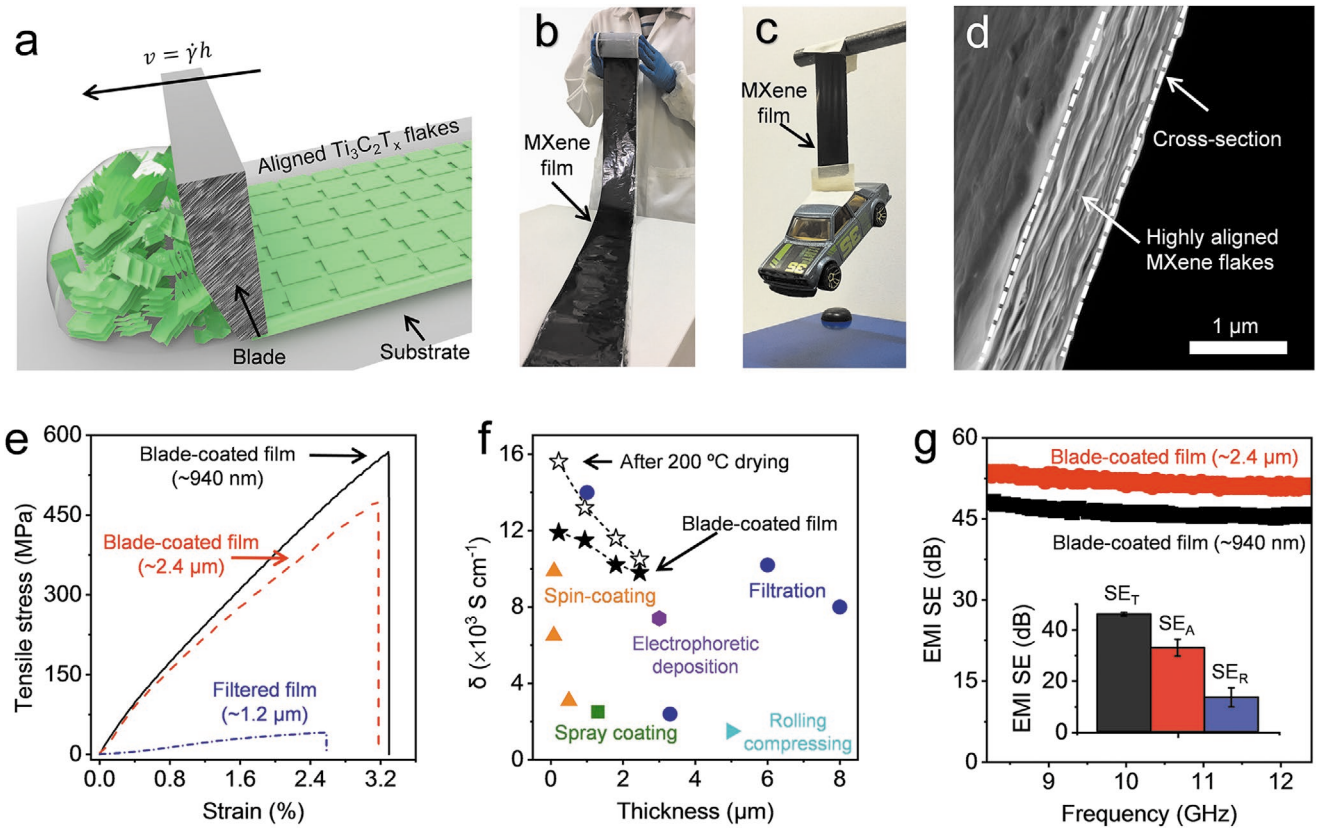


Figure 2. a) Schematic illustration of the blade coating process. b) Digital photograph of a 1 m long and 10 cm wide film produced from large MXene flakes that was blade coated onto a Celgard membrane (thickness of the $Ti_3C_2T_x$ film is 940 nm). c) Digital photograph of a piece of the blade coated $Ti_3C_2T_x$ film (2.0 cm × 6.5 cm, thickness of 940 nm) made from large flakes lifting a ≈40 g object. d) SEM image shows the cross-section of a blade coated film containing highly aligned large MXene flakes. e) Typical stress–strain curves of blade-coated and vacuum-filtered films prepared from large MXene flakes. f) Electrical conductivity of blade-coated large $Ti_3C_2T_x$ films with increasing thickness before and after drying at 200 °C for 6 h. Electrical conductivity and thicknesses of films prepared by spin coating,[14,43,44] spray coating,[13] filtration,[11,16,18,45] electrophoretic deposition,[46] and rolling compressing[31] are plotted for comparison. More references are listed in Table S1 in the Supporting Information. g) EMI shielding effectiveness (SE) performance of blade coated $Ti_3C_2T_x$ film made from large flakes in the X-band (8.2–12.4 GHz). The inset shows the average total EMI SE (SE_T) (≈940 nm) and contribution of absorption (SE_A) and reflection (SE_R) in the X-band.

The large lateral size of MXene flakes resulted in a high aspect ratio ($\langle l\rangle/\langle t\rangle$) of ≈5880, which is ≈50 times larger than that of small flakes ($\langle l\rangle/\langle t\rangle$ ≈120). This high aspect ratio resulted in lyotropic liquid crystals of dispersions of large flakes with a concentration of ≈30 mg mL^{-1}, as observed from their polarized optical microscope images (Figure S3, Supporting Information).The formation of liquid crystal indicates that large MXene flakes self-assembled into oriented domains in the dispersion.[38,39] Rheological measurements also showed that the dispersion of large flakes at 30 mg mL^{-1} presents gel-like viscosity that is as high as 1000 Pa s at 0.01 s^{-1} and the viscosity reduced when the shear rate increased (Figure S4a, Supporting Information). The higher viscosity at a low shear rate and rheological shear-thinning behavior enabled the large MXene dispersion to have excellent processability. Additionally, large MXene flakes also displayed higher elastic (G') and viscous (G'') moduli than that of small flakes at the same concentration (Figure S4b, Supporting Information). The high G'/G'' ratio of large MXene dispersion also reached to ≈10 from 0.01 to 100 Hz, indicating the film morphology will be maintained when the shear force is removed.[40–42] It can be concluded that liquid crystal domains of ordered large MXene flakes can be aligned along the shear direction and the dispersion recovers to the gel state with maintained alignment when the applied shear is removed.

Laboratory-scale vacuum-assisted filtration is the most common method to produce MXene films in the literature; however, a scalable method for film preparation is important to eliminate the variation in properties of MXene films among batches, scaling up the film production, and not to be limited by the filtration setup dimensions. Blade coating is a scalable method used in industrial production of free-standing films and coatings. In this work, we used a blade-coating method to fabricate large area MXene films of varying thicknesses containing highly aligned MXene flakes (**Figure 2**a–c). We controlled the applied shear ($\dot{\gamma}$) to induce the alignment of MXene flakes by adjusting the blade speed (v), i.e., the rate at which we moved the blade from start to finish, and the blade height (h), i.e., the height between the substrate and the blade edge. By precisely controlling the coating procedure, we maintained a shear rate ($\dot{\gamma}$) of 500 s^{-1} by adjusting v and varying h between 38 and 275 μm. The corresponding thicknesses of the

© 2020 WILEY-VCH Verlag GmbH & Co. KGaA, Weinheim

produced MXene films ranged from ≈214 nm to ≈2.4 µm (Table S4 and Figure S5, Supporting Information). The blade coated films had a consistent density of ≈4.3 g cm^{-3}, which was higher than reported values for filtered films and compressed discs from MXene powder (ranging from ≈2.3 to ≈3.8 g cm^{-3}),[3,18] indicating that the blade-coating method leads to highly densified stacking of MXene flakes (Figure S6, Supporting Information). Blade-coated MXene films with thickness above 400 nm can be readily peeled from the Celgard membrane after drying (Figure 2d). To study the effect of flake size on film properties, we prepared blade coated films from a batch of an MXene dispersion containing predominantly large MXene flakes and another containing a dispersion with predominantly small flakes. To probe how varying the degree of alignment and packing density of MXene flakes affect the film properties, we also used the most common vacuum-assisted filtration method to produce MXene films from both large and small flakes.

The tensile stress–strain curves in Figure 2e show the superior tensile strength of blade coated $Ti_3C_2T_x$ films over vacuum-filtered film with the same average flake size. For a representative ≈940 nm blade-coated film, the measured tensile strength of 568 ± 24 MPa is ≈15 times higher than that of the filtered film (≈40 MPa, thickness of 1.2 µm) prepared in this study, five times higher than the best value of previously reported MXene films (112 MPa) and approximately twice that of the best value for MXene-based composite films (341 MPa for MXene/cellulose nanofiber composite film).[22] The tensile strength remained as high as 480 ± 35 MPa for a ≈2.4 µm thick film indicating the excellent connection between large $Ti_3C_2T_x$ flakes. The slight decrease in the strength of the films with increasing film thickness is likely due to the differences in flake alignment. For thick films, it is difficult to maintain the alignment of flakes after drying, which introduces voids between the flakes and results in weak interflake interactions. The weak interflake interactions not only reduce the strength of the films but also decrease their electrical conductivity by reducing the conduction paths. Hence, we believe that the precise control of the alignment of flakes within the film is the key to achieving a combination of high strength and high conductivity. Moreover, all films made from large MXene flakes showed improved tensile strength in comparison with films made from small MXene flakes for both blade coated films and vacuum-assisted filtered films (Table S5, Supporting Information). Additionally, films made from large MXene flakes had around four times higher breaking elongation (≈3.2% for the blade coated film and ≈2.5% for the filtered film) than those made from small MXene flakes (≈0.7% for the blade coated film and ≈1.0% for the filtered film). The higher breaking strain for films made from large MXene flakes could be due to the large flakes providing long distances for flakes to slide passed one another before separating, helping the load transfer inside the film, as observed for other films produced from 2D nanomaterials, such as graphene oxide and clay.[47,48] The close stacking of MXene flakes enabled the blade coated films made from large MXene flakes to have record Young's modulus and toughness of 20.6 GPa and 10.2 MJ m^{-3} (Table S5, Supporting Information), respectively.

The highly oriented MXene flakes in blade coated films also led to very high electrical conductivity with the highest value of 12 300 ± 170 S cm^{-1} measured for a ≈214 nm thin film (Figure 2f). The high electrical conductivity of blade coated films is attributed to the large flake size and improved orientation of flakes in films. The electrical conductivity of blade coated films displayed minimal dependence on film thickness. For example, the electrical conductivity of a ≈2.4 µm thick film (≈11 times the thickness) was 10 200 ± 480 S cm^{-1}. For comparison, a vacuum-filtered film made with large flakes with ≈1.2 µm thickness had a lower electrical conductivity of 9860 ± 180 S cm^{-1}. In an attempt to further improve the electrical conductivity by removing absorbed water from the atmosphere,[49] we treated the $Ti_3C_2T_x$ films under vacuum at 200 °C for 6 h and achieved a record value of 15 100 ± 160 S cm^{-1}, which is the highest conductivity value reported for MXene films. Thermal treatment of blade-coated film at 200 °C has been shown effective in removing the intercalated water molecules between $Ti_3C_2T_x$ flakes.[49] This deintercalation of water molecules leads to decreased interlayer spacing between MXene flakes, as seen in the shift of (002) peak toward higher angle in the XRD data (Figure S7, Supporting Information). It has also been shown that the surface functional groups on $Ti_3C_2T_x$ flakes, such as −OH, −F, and −O, start to decompose at ≈200 °C.[49–51] We have shown that after 6 h of thermal treatment at 200 °C, the water contact angle increased from 45.7° to 73.1°, which could be attributed to the partial removal of surface functional groups. The removal of intercalated molecules leads to a close interconnection between MXene flakes, which offers fast electron transfer. Hence, the thermal treatment is an effective approach to enhance the electrical conductivity of MXene film.

The high electrical conductivity of blade coated films made from large MXene flakes make them excellent candidates for use as an EMI shielding material.[3] We measured the EMI shielding effectiveness (EMI SE) of the films in the X-band (8.2–12.4 GHz) (Figure 2g). A 2.4 µm blade coated film showed a high EMI SE of 53.5 dB at 8.2 GHz, which is comparable with previous reports.[3] Surprisingly, the 940 nm thick film had an EMI SE (47.9 dB at 8.2 GHz), which means >99.99% of the incident microwaves can be blocked by the film. The contribution of absorption (SE_A) and reflection (SE_R) to the total EMI SE (SE_T) is analyzed. As shown in Figure 2g inset, the film showed an average SE_T of 46.1 ± 0.7 dB at the X-band, in which SE_A and SE_R are 32.6 ± 3.3 and 13.5 ± 3.7 dB, respectively. Here high SE_T and SE_A values are related to higher conductivity of blade-coated MXene film. In addition, surface terminations on the MXene films aligned in the direction of applied electric field may undergo polarization, resulting in attenuation by polarization losses.[52] The comparison between film reported in this work and porous films reported in the literature[55] shows that porous MXene foam has a higher SE_A, as shown in Table S6 in the Supporting Information. Porous structure can contribute to microwave absorption owing to enhanced multiple scattering in the foam.[53,54] When the absolute shielding effectiveness is normalized by film thickness (SSE/t),[3] the SSE/t of blade coated MXene film using large flakes (≈1.2×10^5 dB cm^2 g^{-1}) was higher than most of MXene-based films and approached the highest reported value for a 60 µm thick MXene foam (≈1.3×10^5 dB cm^2 g^{-1}) (Figure S8, Supporting Information).[55] As demonstrated in previous studies,[53] increasing the porosity of a MXene film can further increase the SE_A and the SE_T up to

© 2020 WILEY-VCH Verlag GmbH & Co. KGaA, Weinheim

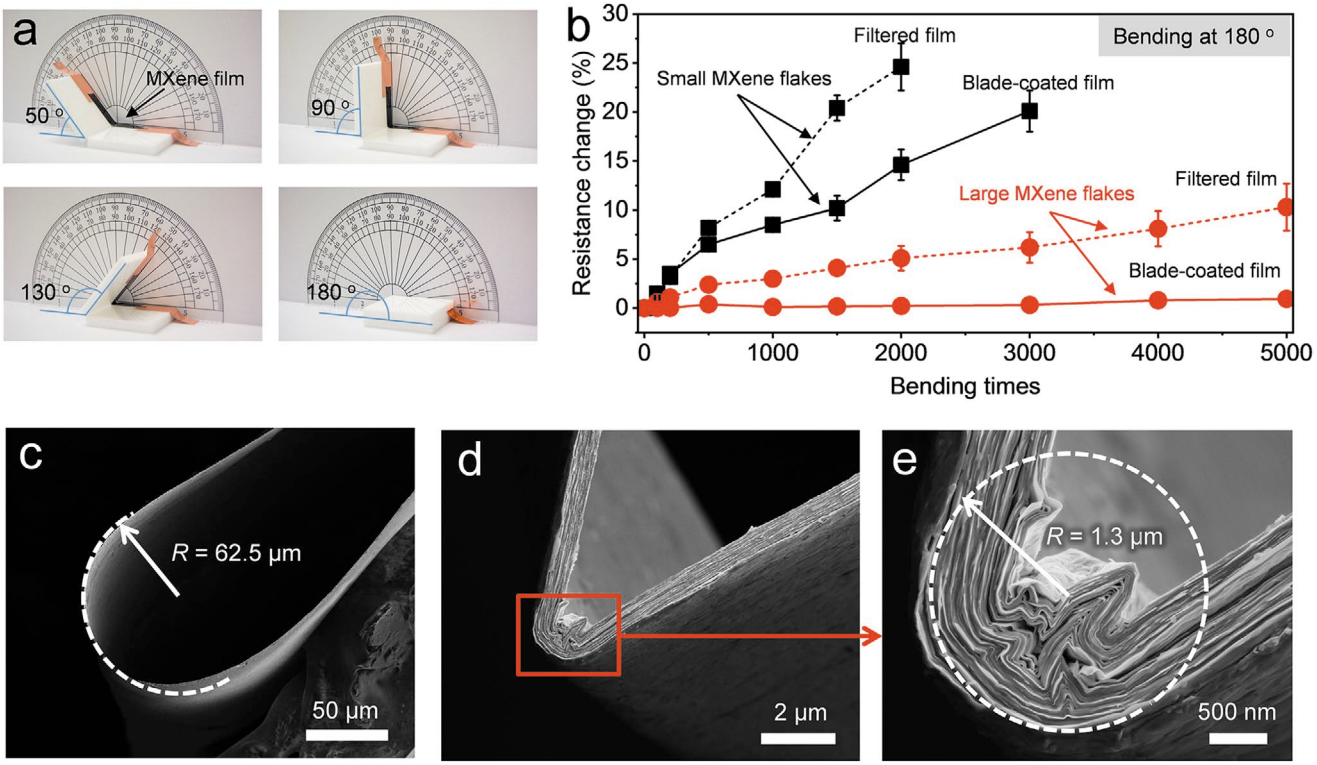


Figure 3. a) Photos of a piece of MXene film (1 cm × 4 cm) undergoing a bend test. The film is mounted on two insulating poly(tetrafluoroethylene) blocks which can be repeatedly bent at various degrees. Conducting copper tapes were used at both ends of the sample to establish the electrical connection. b) Changes in resistance of MXene film after fully folded (180°) for up to 5000 cycles. Filtered and blade-coated films that are made from small flakes are broken after bending for ≈2000 and ≈3000 cycles, respectively. c) SEM image of blade coated film made from large flakes folded at 180° forming a radius of ≈62.5 µm. d,e) Low-magnification (d) and e) high-magnification (e) SEM images of a blade coated film made from large flakes bent at an extremely small radius of ≈1.3 µm.

70 dB. However, highly porous structures lead to poor interconnection between flakes, which cannot meet the requirement for high mechanical strength. The film developed in this study is multifunctional, free-standing and can be applied to a variety of surfaces, providing sufficient shielding effectiveness for many applications such as microelectronics or wearables, where sub-micrometer shielding layers are needed.

Besides the unprecedented tensile strength and electrical conductivity, the blade-coated films exhibited excellent flexibility and stable resistance after repeated bending cycles. For example, after bending at 180° for 500 cycles using a custom designed device (**Figure 3**a), the blade coated film made from large MXene flakes showed a minimal increase in resistance (≈0.4%) while the resistance of the filtered MXene film using large flakes increased by ≈2.5% (Figure S9, Supporting Information). Extending the bending cycles to 5000 revealed <1% increase in resistance of blade coated films made from large flakes when bent at 180° (Figure 3b). The resistance of a filtered film made from large flakes increased by 12% after 5000 bending cycles and the filtered film made from small flakes broke after ≈2000 cycles. SEM examination of the blade coated film made from large flakes bent at 180°, corresponding to a bending radius of 62.5 µm, revealed an internal morphology that consisted of compact stacks of highly aligned MXene flakes along the film plane (Figure 3c). When the bending radius of film is further reduced, the large $Ti_3C_2T_x$ flakes remained tightly stacked, even at a radius of curvature of 1.3 µm (Figure 3d,e). We observed minimal buckling of large flakes localized on the inner side of the curved surface due to the compressive stress imposed during bending. In contrast, multiple creases were observed for the filtered film even at a significantly larger bending radius of ≈68.1 µm (Figure S10, Supporting Information). These results clearly illustrate that large MXene flakes and improved alignment along the film plane enhanced the connectivity between flakes within the films.

We also used small- and wide-angle X-ray scattering (SAXS/WAXS) measurements to elucidate how MXene flakes are oriented in blade coated and filtered films using large $Ti_3C_2T_x$ flakes. As shown in **Figure 4**a, measurements were carried out at two X-ray beam orientations (parallel and perpendicular) relative to the film plane. With the parallel configuration, while both films showed scattering pattern along the q_y direction (Figure 4b,c), the blade coated film revealed a narrower (002) peak when the integrated signals were normalized by the intensity of (002) peak (Figure 4f). These results suggest that blade coating led to more uniformly spaced flakes than vacuum-assisted filtration. To study the orientation of the unit cells of $Ti_3C_2T_x$ in the film plane, we compared the azimuthal plots of the (002) peak, which represent the normal directions of the flake plane, of films produced by blade coating and vacuum-assisted filtration (Figure 4g). Here, we adopted Herman's orientation factor (f), an indicator widely used for the analysis of

© 2020 WILEY-VCH Verlag GmbH & Co. KGaA, Weinheim

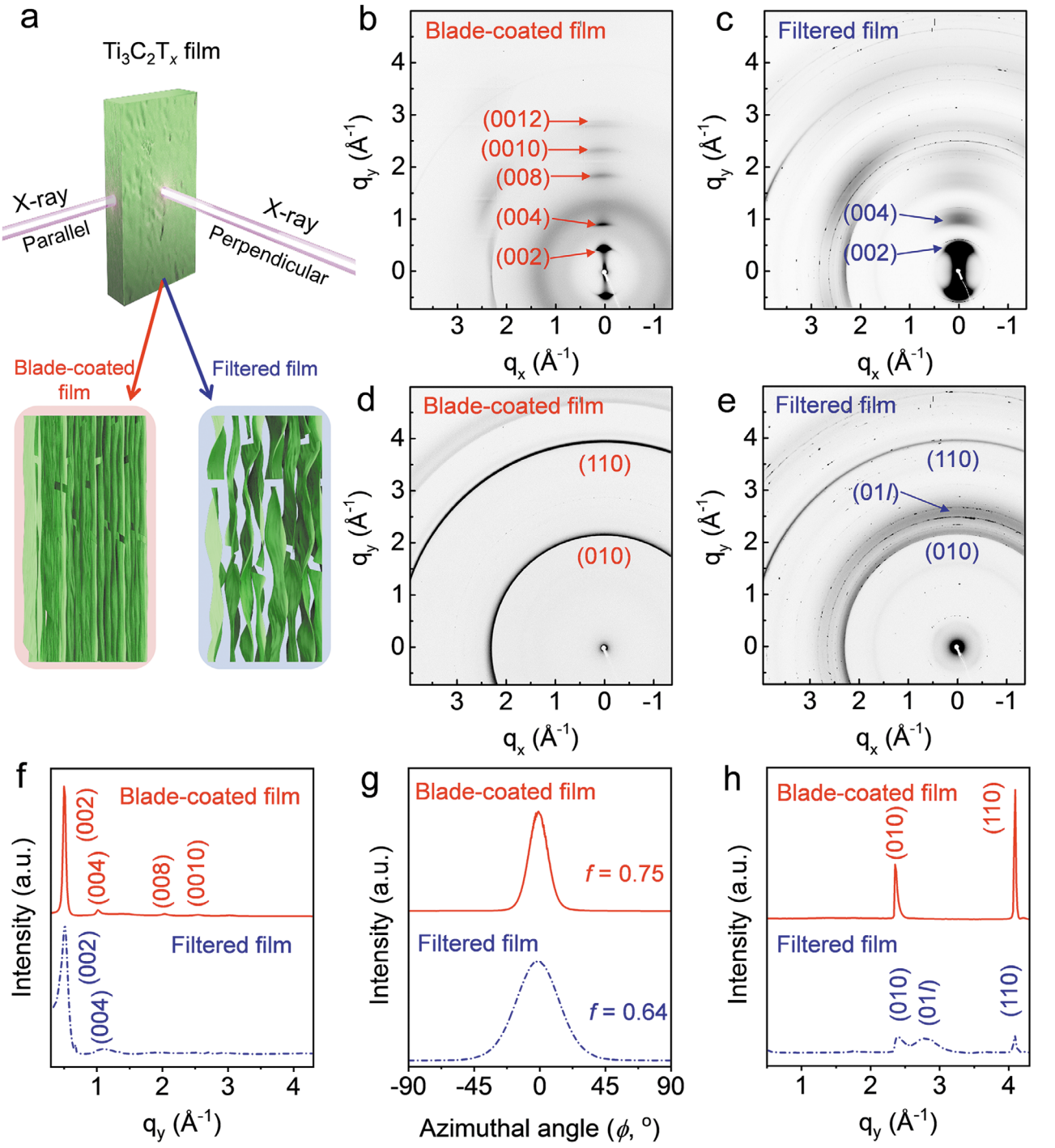


Figure 4. a) Schematic illustration of the positions of the X-ray beam (parallel and perpendicular to the MXene film plane) during small- and wide-angle X-ray scattering (SAXS/WAXS). The bottom shows the predicated microstructure and orientation of MXene flakes within films produced by blade coating and vacuum-assisted filtration. b,c) SAXS/WAXS patterns of blade-coated films (b) and filtered films (c) prepared using large MXene flakes when the film plane is parallel to the X-ray beam. d,e) SAXS/WAXS patterns of blade-coated films (d) and filtered films (e) prepared using large MXene flakes when the film plane is perpendicular to the X-ray beam. f) Diffractograms of the film samples obtained by integration of SAXS/WAXS 2D spectra shown in (a) and (b) along the q_y direction. g) Azimuthal plot for (002) peaks marked in (a) and (b) in azimuth range of −90° and 90°. h) Diffractograms of MXene films obtained by integration of (c) and (d) along the q_y direction.

polymer alignment,[56] to assess the orientation of flakes relative to the film plane (see calculation details in the Supporting Information). The orientation factor value ranges from 0 to 1, which indicates random to full alignment with respect to the axis of interest, respectively. As shown in Figure 4g, we found that the orientation factor for a blade coated film (0.75) was

© 2020 WILEY-VCH Verlag GmbH & Co. KGaA, Weinheim

higher than that for a filtered film (0.64) suggesting increased anisotropy when large $Ti_3C_2T_x$ flakes were aligned by shear (blade-coating method) compared to self-assembly (filtration method). We also analyzed the data obtained from the perpendicular test configuration. It is noteworthy that this configuration enabled the detection of the (010) and (110) planes of the *P6₃/mmc* unit cells of $Ti_3C_2T_x$ for both samples (Figure 4d,e), which cannot be observed in the parallel test configuration. Only two distinct concentric patterns were observed for the blade coated film, which indicate that the MXene flakes lie parallel to the film plane with minimum disorientation. In contrast, the intensity of the (010) and (110) peaks significantly decreased and several (01*l*) scattering peaks attributed to (011), (013), (014), and (016) planes were evident for the filtered film (Figure 4h). The peaks observed at around q_y = 2.78 Å^{-1} indicate that the *P6₃/mmc* unit cells of flakes have slopes between the film plane, suggesting MXene flakes are stacking wrinkly in the filtered films. Based on these results, we infer that during the formation of films, MXene flakes are parallel to the film surface in blade coated films, while flakes are present as partly isotropic regions in filtered films. Such regional disorders in filtered films may be ascribed to the misalignment and/or wrinkling of the large MXene flakes that are not easily eliminated by the filtration process unlike in blade coating where the application of shear induces the alignment of flakes. These results collectively support the observed superior electrical and mechanical properties of blade coated films made from large MXene flakes.

Here we demonstrated that the quality of MXene dispersion is necessary to produce MXene films that display both high strength and high conductivity. Production of high-quality MXene dispersions in large quantity (≈50 g per batch) has been recently demonstrated,[57] paving the way for the large-scale manufacturing of high quality MXene films. It is envisaged that future scaling up of film production will involve automation of the film processing parameters (i.e., blade speed, height, and force for a uniform and constant shear rate) to ensure the consistent production of high quality films. It will also involve both online and offline tests/measurements (i.e., electrical resistance, mechanical properties, etc.) to monitor the film properties.

In summary, we have demonstrated that it is possible to achieve both high strength and enhanced electrical conductivity of pure $Ti_3C_2T_x$ MXene films using large size MXene flakes and a scalable blade coating process. High aspect ratio MXene flakes were firstly synthesized by preselecting the large MAX phase and then adjusting the etching conditions. Additionally, the formation of liquid crystalline MXene and proper rheological properties of dispersion enabled the alignment of flakes under shear force, leading to highly orientated flakes along the blade-coated film plane. These combined metrics resulted in free-standing thin films with record tensile strength (≈570 MPa), Young's modulus (≈20.6 GPa), and high electrical conductivity of ≈15 100 S cm^{-1} (after annealing treatment). The positive effect of large MXene flakes and their alignment on mechanical properties and electrical conductivity is expected to enable the development of a range of applications based on strong and conductive pure MXene films, such as EMI shielding, energy storage, and printed electronics.

Supporting Information

Supporting Information is available from the Wiley Online Library or from the author.

Acknowledgements

The authors acknowledge financial support from the Australian Research Council (FT130100380, IH140100018, and DP170102859) and Deakin University (Alfred Deakin Postdoctoral Research Fellowship Scheme). The authors also acknowledge the Australian Synchrotron facility (Melbourne) for the use of the SAXS/WAXS beamline and the Australian National Fabrication Facility (ANFF) Victorian nodes at La Trobe and Deakin Universities. A.L. acknowledges support from the U.S. National Science Foundation Graduate Research Fellowship under Grant No. DGE-1646737. The authors would like to thank Asia Sarycheva (Drexel University) for discussion on the Raman data.

Conflict of Interest

The authors declare no conflict of interest.

Keywords

aligned films, electrical conductivity, electromagnetic interference shielding, MXene films

Received: February 16, 2020
Published online: April 20, 2020

[1] B. Anothumakkool, R. Soni, S. N. Bhange, S. Kurungot, *Energy Environ. Sci.* **2015**, *8*, 1339.
[2] Z. Xiong, C. Liao, W. Han, X. Wang, *Adv. Mater.* **2015**, *27*, 4469.
[3] F. Shahzad, M. Alhabeb, C. B. Hatter, B. Anasori, S. Man Hong, C. M. Koo, Y. Gogotsi, *Science* **2016**, *353*, 1137.
[4] Z. Liu, H. Wang, P. Huang, J. Huang, Y. Zhang, Y. Wang, M. Yu, S. Chen, D. Qi, T. Wang, Y. Jiang, G. Chen, G. Hu, W. Li, J. Yu, Y. Luo, X. J. Loh, B. Liedberg, G. Li, X. Chen, *Adv. Mater.* **2019**, *31*, 1901360.
[5] W. A. D. M. Jayathilaka, K. Qi, Y. Qin, A. Chinnappan, W. Serrano-García, C. Baskar, H. Wang, J. He, S. Cui, S. W. Thomas, S. Ramakrishna, *Adv. Mater.* **2019**, *31*, 1805921.
[6] Y. Yang, X. Yang, L. Liang, Y. Gao, H. Cheng, X. Li, M. Zou, R. Ma, Q. Yuan, X. Duan, *Science* **2019**, *364*, 1057.
[7] S. Wan, S. Fang, L. Jiang, Q. Cheng, R. H. Baughman, *Adv. Mater.* **2018**, *30*, 1802733.
[8] B. Anasori, Y. Gogotsi, in *2D Metal Carbides and Nitrides (MXenes): Structure, Properties and Applications*, Springer International Publishing, Cham, Switzerland **2019**.
[9] G. Deysher, C. E. Shuck, K. Hantanasirisakul, N. C. Frey, A. C. Foucher, K. Maleski, A. Sarycheva, V. B. Shenoy, E. A. Stach, B. Anasori, Y. Gogotsi, *ACS Nano* **2020**, *14*, 204.
[10] M. R. Lukatskaya, S. Kota, Z. Lin, M.-Q. Zhao, N. Shpigel, M. D. Levi, J. Halim, P.-L. Taberna, M. W. Barsoum, P. Simon, Y. Gogotsi, *Nat. Energy* **2017**, *2*, 17105.
[11] S. A. Mirkhani, A. Shayesteh Zeraati, E. Aliabadian, M. Naguib, U. Sundararaj, *ACS Appl. Mater. Interfaces* **2019**, *11*, 18599.
[12] K. Maleski, V. N. Mochalin, Y. Gogotsi, *Chem. Mater.* **2017**, *29*, 1632.
[13] Y.-Y. Peng, B. Akuzum, N. Kurra, M.-Q. Zhao, M. Alhabeb, B. Anasori, E. C. Kumbur, H. N. Alshareef, M.-D. Ger, Y. Gogotsi, *Energy Environ. Sci.* **2016**, *9*, 2847.

 © 2020 WILEY-VCH Verlag GmbH & Co. KGaA, Weinheim

[14] C. Zhang, B. Anasori, A. Seral-Ascaso, S.-H. Park, N. McEvoy, A. Shmeliov, G. S. Duesberg, J. N. Coleman, Y. Gogotsi, V. Nicolosi, *Adv. Mater.* **2017**, *29*, 1702678.
[15] A. Lipatov, H. Lu, M. Alhabeb, B. Anasori, A. Gruverman, Y. Gogotsi, A. Sinitskii, *Sci. Adv.* **2018**, *4*, eaat0491.
[16] H. Chen, Y. Wen, Y. Qi, Q. Zhao, L. Qu, C. Li, *Adv. Funct. Mater.* **2019**, *29*, 1906996.
[17] Z. Zhan, Q. Song, Z. Zhou, C. Lu, *J. Mater. Chem. C* **2019**, *7*, 9820.
[18] Z. Ling, C. E. Ren, M.-Q. Zhao, J. Yang, J. M. Giammarco, J. Qiu, M. W. Barsoum, Y. Gogotsi, *Proc. Natl. Acad. Sci. U. S. A.* **2014**, *111*, 16676.
[19] J. Lipton, G. M. Weng, M. Alhabeb, K. Maleski, F. Antonio, J. Kong, Y. Gogotsi, A. D. Taylor, *Nanoscale* **2019**, *11*, 20295.
[20] J.-Q. Luo, S. Zhao, H.-B. Zhang, Z. Deng, L. Li, Z.-Z. Yu, *Compos. Sci. Technol.* **2019**, *182*, 107754.
[21] W.-T. Cao, F.-F. Chen, Y.-J. Zhu, Y.-G. Zhang, Y.-Y. Jiang, M.-G. Ma, F. Chen, *ACS Nano* **2018**, *12*, 4583.
[22] W. Tian, A. VahidMohammadi, M. S. Reid, Z. Wang, L. Ouyang, J. Erlandsson, T. Pettersson, L. Wagberg, M. Beidaghi, M. M. Hamedi, *Adv. Mater.* **2019**, *31*, 1902977.
[23] Y. Wang, X. Wang, X. Li, Y. Bai, H. Xiao, Y. Liu, R. Liu, G. Yuan, *Adv. Funct. Mater.* **2019**, *29*, 1900326.
[24] F. Xie, F. Jia, L. Zhuo, Z. Lu, L. Si, J. Huang, M. Zhang, Q. Ma, *Nanoscale* **2019**, *11*, 23382.
[25] Z. Zhang, S. Yang, P. Zhang, J. Zhang, G. Chen, X. Feng, *Nat. Commun.* **2019**, *10*, 2920.
[26] J. Liu, Z. Liu, H.-B. Zhang, W. Chen, Z. Zhao, Q.-W. Wang, Z.-Z. Yu, *Adv. Electron. Mater.* **2019**, *5*, 1901094.
[27] W. Tian, A. VahidMohammadi, M. S. Reid, Z. Wang, L. Ouyang, J. Erlandsson, T. Pettersson, L. Wågberg, M. Beidaghi, M. M. Hamedi, *Adv. Mater.* **2019**, *31*, 1902977.
[28] M. Alhabeb, K. Maleski, B. Anasori, P. Lelyukh, L. Clark, S. Sin, Y. Gogotsi, *Chem. Mater.* **2017**, *29*, 7633.
[29] K. Maleski, C. E. Ren, M.-Q. Zhao, B. Anasori, Y. Gogotsi, *ACS Appl. Mater. Interfaces* **2018**, *10*, 24491.
[30] A. Lipatov, M. Alhabeb, M. R. Lukatskaya, A. Boson, Y. Gogotsi, A. Sinitskii, *Adv. Electron. Mater.* **2016**, *2*, 1600255.
[31] M. Ghidiu, M. R. Lukatskaya, M.-Q. Zhao, Y. Gogotsi, M. W. Barsoum, *Nature* **2014**, *516*, 78.
[32] X. Wang, X. Shen, Y. Gao, Z. Wang, R. Yu, L. Chen, *J. Am. Chem. Soc.* **2015**, *137*, 2715.
[33] W. Bao, L. Liu, C. Wang, S. Choi, D. Wang, G. Wang, *Adv. Energy Mater.* **2018**, *8*, 1702485.
[34] C. J. Zhang, S. Pinilla, N. McEvoy, C. P. Cullen, B. Anasori, E. Long, S.-H. Park, A. Seral-Ascaso, A. Shmeliov, D. Krishnan, C. Morant, X. Liu, G. S. Duesberg, Y. Gogotsi, V. Nicolosi, *Chem. Mater.* **2017**, *29*, 4848.
[35] B. Ahmed, D. H. Anjum, M. N. Hedhili, Y. Gogotsi, H. N. Alshareef, *Nanoscale* **2016**, *8*, 7580.
[36] A. Sarycheva, T. Makaryan, K. Maleski, E. Satheeshkumar, A. Melikyan, H. Minassian, M. Yoshimura, Y. Gogotsi, *J. Phys. Chem. C* **2017**, *121*, 19983.
[37] T. Hu, J. Wang, H. Zhang, Z. Li, M. Hu, X. Wang, *Phys. Chem. Chem. Phys.* **2015**, *17*, 9997.
[38] Y. Xia, T. S. Mathis, M.-Q. Zhao, B. Anasori, A. Dang, Z. Zhou, H. Cho, Y. Gogotsi, S. Yang, *Nature* **2018**, *557*, 409.
[39] J. Zhang, S. Uzun, S. Seyedin, P. A. Lynch, B. Akuzum, Z. Wang, S. Qin, M. Alhabeb, C. E. Shuck, W. Lei, E. C. Kumbur, W. Yang, X. Wang, G. Dion, J. M. Razal, Y. Gogotsi, *ACS Cent. Sci.* **2020**, *6*, 254.
[40] Y. Li, T. Gao, Z. Yang, C. Chen, W. Luo, J. Song, E. Hitz, C. Jia, Y. Zhou, B. Liu, B. Yang, L. Hu, *Adv. Mater.* **2017**, *29*, 1700981.
[41] W. Yang, J. Yang, J. J. Byun, F. P. Moissinac, J. Xu, S. J. Haigh, M. Domingos, M. A. Bissett, R. A. W. Dryfe, S. Barg, *Adv. Mater.* **2019**, *31*, 1902725.
[42] R. Jalili, S. H. Aboutalebi, D. Esrafilzadeh, K. Konstantinov, J. M. Razal, S. E. Moulton, G. G. Wallace, *Mater. Horiz.* **2014**, *1*, 87.
[43] A. D. Dillon, M. J. Ghidiu, A. L. Krick, J. Griggs, S. J. May, Y. Gogotsi, M. W. Barsoum, A. T. Fafarman, *Adv. Funct. Mater.* **2016**, *26*, 4162.
[44] M. Mariano, O. Mashtalir, F. Q. Antonio, W.-H. Ryu, B. Deng, F. Xia, Y. Gogotsi, A. D. Taylor, *Nanoscale* **2016**, *8*, 16371.
[45] A. Sarycheva, A. Polemi, Y. Liu, K. Dandekar, B. Anasori, Y. Gogotsi, *Sci. Adv.* **2018**, *4*, eaau0920.
[46] P. Collini, S. Kota, A. D. Dillon, M. W. Barsoum, A. T. Fafarman, *J. Electrochem. Soc.* **2017**, *164*, D573.
[47] J. Chen, Y. Li, L. Huang, N. Jia, C. Li, G. Shi, *Adv. Mater.* **2015**, *27*, 3654.
[48] P. Podsiadlo, A. K. Kaushik, E. M. Arruda, A. M. Waas, B. S. Shim, J. Xu, H. Nandivada, B. G. Pumplin, J. Lahann, A. Ramamoorthy, N. A. Kotov, *Science* **2007**, *318*, 80.
[49] J. L. Hart, K. Hantanasirisakul, A. C. Lang, B. Anasori, D. Pinto, Y. Pivak, J. T. van Omme, S. J. May, Y. Gogotsi, M. L. Taheri, *Nat. Commun.* **2019**, *10*, 522.
[50] O. Mashtalir, M. R. Lukatskaya, A. I. Kolesnikov, E. Raymundo-Pinero, M. Naguib, M. W. Barsoum, Y. Gogotsi, *Nanoscale* **2016**, *8*, 9128.
[51] M. Seredych, C. E. Shuck, D. Pinto, M. Alhabeb, E. Precetti, G. Deysher, B. Anasori, N. Kurra, Y. Gogotsi, *Chem. Mater.* **2019**, *31*, 3324.
[52] B. Wen, M. Cao, M. Lu, W. Cao, H. Shi, J. Liu, X. Wang, H. Jin, X. Fang, W. Wang, J. Yuan, *Adv. Mater.* **2014**, *26*, 3484.
[53] J. Liu, H.-B. Zhang, R. Sun, Y. Liu, Z. Liu, A. Zhou, Z.-Z. Yu, *Adv. Mater.* **2017**, *29*, 1702367.
[54] M. Han, X. Yin, K. Hantanasirisakul, X. Li, A. Iqbal, C. B. Hatter, B. Anasori, C. M. Koo, T. Torita, Y. Soda, L. Zhang, L. Cheng, Y. Gogotsi, *Adv. Opt. Mater.* **2019**, *7*, 1900267.
[55] J. Liu, H.-B. Zhang, R. Sun, Y. Liu, Z. Liu, A. Zhou, Z.-Z. Yu, *Adv. Mater.* **2017**, *29*, 1702367.
[56] J. Zhang, S. Seyedin, S. Qin, P. A. Lynch, Z. Wang, W. Yang, X. Wang, J. M. Razal, *J. Mater. Chem. A* **2019**, *7*, 6401.
[57] C. E. Shuck, A. Sarycheva, M. Anayee, A. Levitt, Y. Zhu, S. Uzun, V. Balitskiy, V. Zahorodna, O. Gogotsi, Y. Gogotsi, *Adv. Eng. Mater.* **2020**, *22*, 1901241.

© 2020 WILEY-VCH Verlag GmbH & Co. KGaA, Weinheim